

# Comparison between SPT and PT for defect characterization of CFRP plates glued on concrete or wood structures using optical active infrared thermography

by A. Crinière\*, J. Dumoulin\*, C. Ibarra-Castanedo\*\*, L-D. Theroux\*,\*\* and X. Maldague\*\*

\* LUNAM Université, IFSTTAR, MACS, F-44340, Bouguenais, France, {[jean.dumoulin](mailto:jean.dumoulin@ifsttar.fr), [antoine.criniere](mailto:antoine.criniere@ifsttar.fr)}@ifsttar.fr}

\*\* Computer Vision and Systems Laboratory, Pavillon Adrien-Pouliot, Laval University, Quebec (PQ) Canada, G1V 0V6, {[Clemente.Ibarra-Castanedo](mailto:Clemente.Ibarra-Castanedo@gel.ulaval.ca), [louis-daniel.theroux.1,MaldagX](mailto:louis-daniel.theroux.1,MaldagX}@gel.ulaval.ca)}@gel.ulaval.ca}

## Abstract

The objectives of the study summarized hereafter are to compare square pulse and pulsed thermography for defect detection and characterization of CFRP plates used as structural reinforcement in Civil Engineering applications. Image processing and an inverse method coupled with thermal quadrupoles model are also studied.

## 1. Introduction

Strengthening or retrofitting of reinforced concrete structures by externally bonded Fiber Reinforced Polymer (FRP) systems is now a commonly accepted and widespread technique. However, the use of bonding techniques always implies following rigorous installation procedures [1-3]. Moreover professional crews have to be trained in accordance to ensure the durability and long-term performance of the FRP reinforcements. Conformity checking through an "in situ" verification of the bonded FRP systems is then highly desirable. The quality-control program should involve a set of adequate inspections and tests. Visual inspection and acoustic sounding (hammer tap) are commonly used to detect delaminations (disbonds). Nevertheless, these techniques are unable to provide sufficient information about the depth (in case of multilayered composite) and width of disbanded areas and are not capable of evaluating the degree of adhesion between the FRP and the substrate (partial delamination, damage of the resin, poor mechanical properties of the resin). Consequently, rapid and efficient inspection methods are required. Among the non destructive methods under study, active infrared thermography is investigated [4] due to its ability to be used in the field. In the present study we investigate two thermal excitation approaches on 3 different samples built in laboratory. They include defects at different depths with different thermal properties and sizes. Image processing and inverse thermal modelling based on 1D multi-layered thermal quadrupoles are presented for defective areas and glue layer thickness characterization. Processing approaches are first studied using numerical simulation and then applied to experimental data obtained in laboratory.

## 2. Experimental set-up and numerical simulations

### 2.1. Sample characteristics

Samples were reinforced with CFRP plates (provided by SIKA Canada) externally bonded on concrete blocks and wood plank. Various types of defects (wood, steel, Teflon, cork...) were inserted in the glue layer during fabrication up to air voids in the support layer (i.e. wood plank). Fig. 1 shows photographs of the samples fabricated in laboratory.



Car I and Car II samples



Wood\_car Sample

**Fig. 1.** View of the realized samples with their respective defects before gluing CFRP plates on concrete block (upper pictures) and on wood plank (lower pictures)

In the two Car samples, defects are a Teflon disk, cork and steel squares of two different extensions but with same thickness, and a wood rectangle. For wood\_car sample, defects are made of Teflon sticks located between CFRP and glue and between glue and wood plank. Furthermore, 3 air gaps with cross shape were added at wood plank level.

Figure 2 shows the distribution of faults in the sample Wood\_Car.

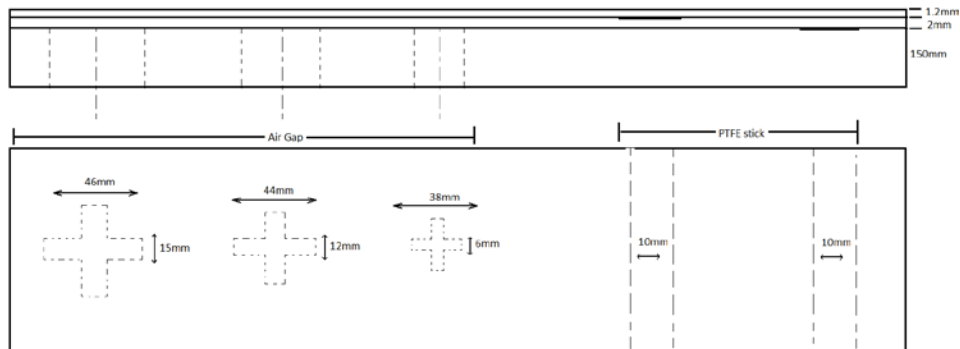


**Fig. 2.** View of the 3 layers wood sample, flaw map

The main characteristics of CFRP plates (Carbodur 1012 provided by SIKA Canada), epoxy resin and cement concrete are reported in Table 1, which also reports the thermal properties taken into account for defects.

**Table 1.** Main characteristics and thermal properties of the constitutive elements of the samples.

Material	Geometric characteristics	$k (W.m^{-1}.K^{-1})$	$\rho (kg.m^{-3})$	$C_p (J.kg^{-1}.K^{-1})$
SIKA Carbodur 1012 (CFRP)	460 mm (L) x 100 mm (W) x 1.2 mm (D)	4.2    fibers 0.7 $\perp$ fibers	1530	840
Epoxy resin : Sikadur - 30	460 mm (L) x 170 mm (W) x ~1 mm (D)	0.2	1200	1220
Cement concrete block	460 mm (L) x 170 mm (W) x 100 mm (D)	1.8	2300	920
Wood	20 mm (L) x 10 mm (W) x 1 mm (D)	0.15	600	1900
Steel	40 mm (L) x 40 mm (W) x 1 mm (D)	15.1	8055	480
Teflon	20 mm (Diameter) x 1 mm (D) + figure 2	0.235	2200	1050
Cork	20 mm(L) x 40 mm (W) x 1 mm (D)	0.039	120	1800
Air	See figure 2 and figure 3	0.0242	1.225	1006

## 2.2. Experimental test bench

Samples were submitted to two types of thermal excitation. The first one was a short pulse heat stimulation using two "BALCAR" flashes of 6,400 J with a pulse duration of 10 ms. The second one was a long square heating pulse of 30 s using two halogen lamps of 1,000 W each. For both configurations distance between the sample and the lamps was 1 m. Lamps were positioned at a 45° angle for both pulsed and square heating. A schematic representation of the test bench is presented in Fig. 3.

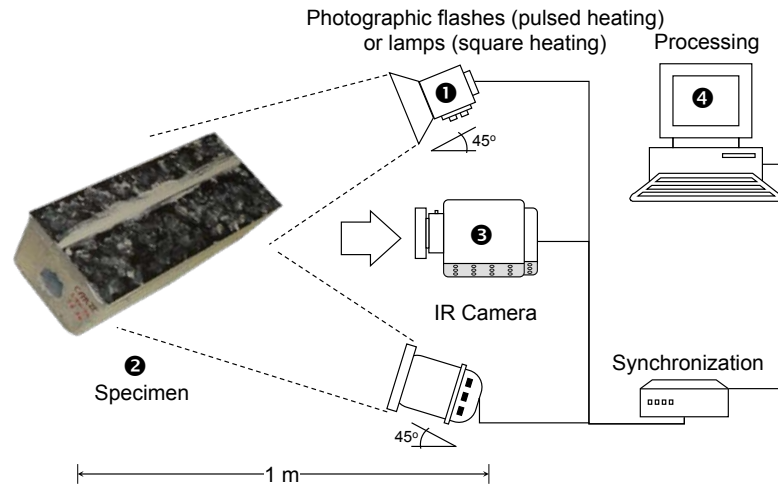


**Fig. 3.** Scheme of the laboratory test bench.

A FLIR MWIR IRFPA camera (Phoenix, InSb, 3-5  $\mu\text{m}$ , 640 X 512 pixels), was used during trials. For pulse excitation thermal image acquisition frequency was set to 22Hz for samples CAR I and II. For square heating excitation acquisition frequency used was of 5.5 Hz for the 30 s step on samples CAR I and II and 9.6 Hz for 120s step on wood\_car sample.

### 2.3. Numerical simulations

Numerical simulations were accomplished using Finite Element Method (FEM). A 3D model of a cement concrete parallelepiped block was performed under COMSOL. Different defects were inserted on the surface of this block (see Fig. 4a). The block size is the same as the laboratory samples and its depth is 4 cm, which is sufficiently thick to assume that its rear face would not be affected by the thermal wave generated by the two kinds of thermal stimulation studied herein.

As for the experimental samples, CFRP plates with same characteristics were inserted on top of the concrete block. An epoxy resin layer of 1 mm between the concrete and CFRP plates was considered. A gap of 10 mm compound filled with epoxy resin was left between the two plates.

For the numerical simulation 3 defect geometries were considered: rectangular, square and circular, all with a thickness of 1 mm. An illustration of the geometry and of the mesh is given in Fig. 4b for various defects inserted between CFRP and concrete.

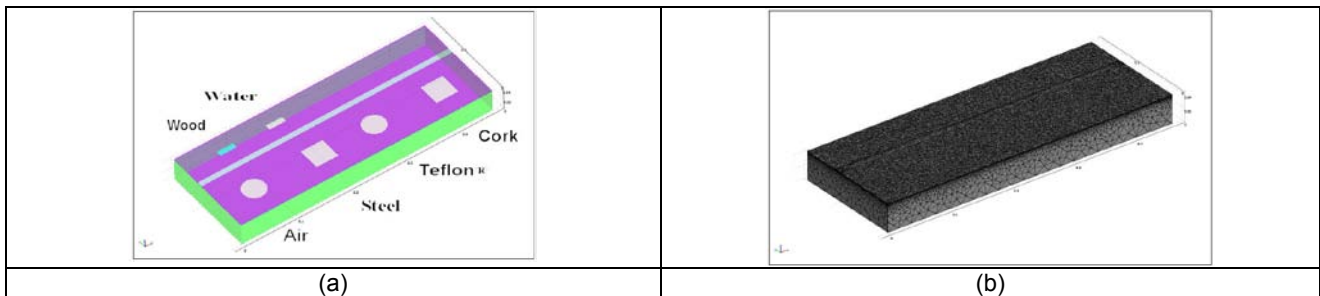


**Fig. 4.** Illustration of numerical simulation: (a) distribution of different defect types, and (b) FE meshing made with COMSOL.

The influence of the thermal excitation type (pulse or square pulse heating), for different numerical configurations, was studied in terms of time evolution of the defect thermal signature. No additional thermal resistance at the interfaces were considered for numerical simulations. The thermal signatures of the different kinds of defects numerically inserted in the glue layer between the concrete substrate and the FRP composite were also simulated. The 3 defect geometries designed for numerical simulations have the same dimensions independently of their nature. The thickness of all defects was 1 mm, which is the same as the resin epoxy layer. The disk defect has a diameter of 40 mm, the rectangle defect size is 30 mm (L) x 10 mm (W) and the size of the square defect side is 40 mm.

The block was assumed to be insulated on its lateral faces. The first type of boundary condition was fixed on the concrete block's rear surface (temperature was 293.15 K). Front face (CFRP) was submitted to a heat pulse and in a first approximation a mean heat transfer coefficient of 10  $\text{W}\cdot\text{m}^{-2}\cdot\text{C}$  was included to the boundary conditions for this face. Thermal properties reported in Table 1 were used for computation.

It should be noticed that for all simulations no contact thermal resistance was considered between upper and lower boundaries of defects.

### 3. Experimental and simulated thermograms - Defect detection and mapping

#### 3.1. Simulated and experimental thermograms

Fig. 5 shows the thermal profiles for defective and non-defective (sound) areas obtained by numerical simulations for 10 ms pulse heating and 30 s square heating. As can be seen from these profiles, cork and wood defects produce a positive thermal contrast with respect to the sound area. On the contrary, steel and Teflon® produce a negative contrast.

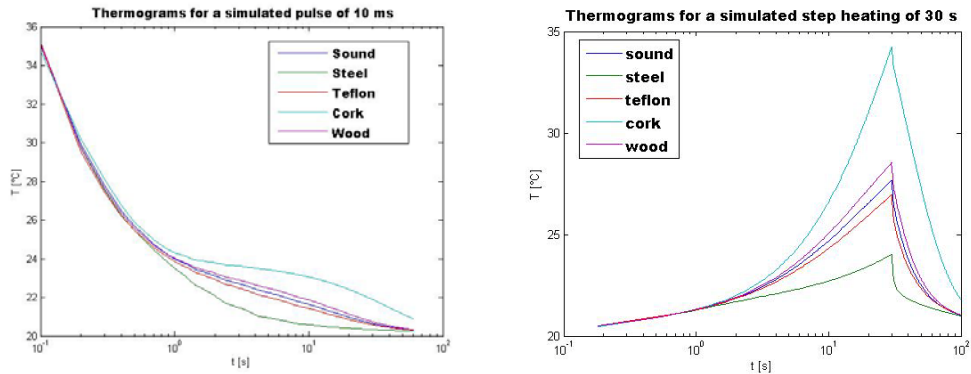


Fig. 5. Pulse (left) and square pulse heating (right) thermograms extracted from numerical simulations.

Figure 6 shows the experimental thermal profiles for the different samples, Car I (left), Car II (middle) and wood\_car (right) for the pulsed heating (top) and the square heating (bottom) experiments. The specimen Car I contained steel and wood type defects, whilst specimen Car II contained cork and Teflon® type defects. Sound areas next to these defects were selected in order to minimize the effect of non-uniformities.

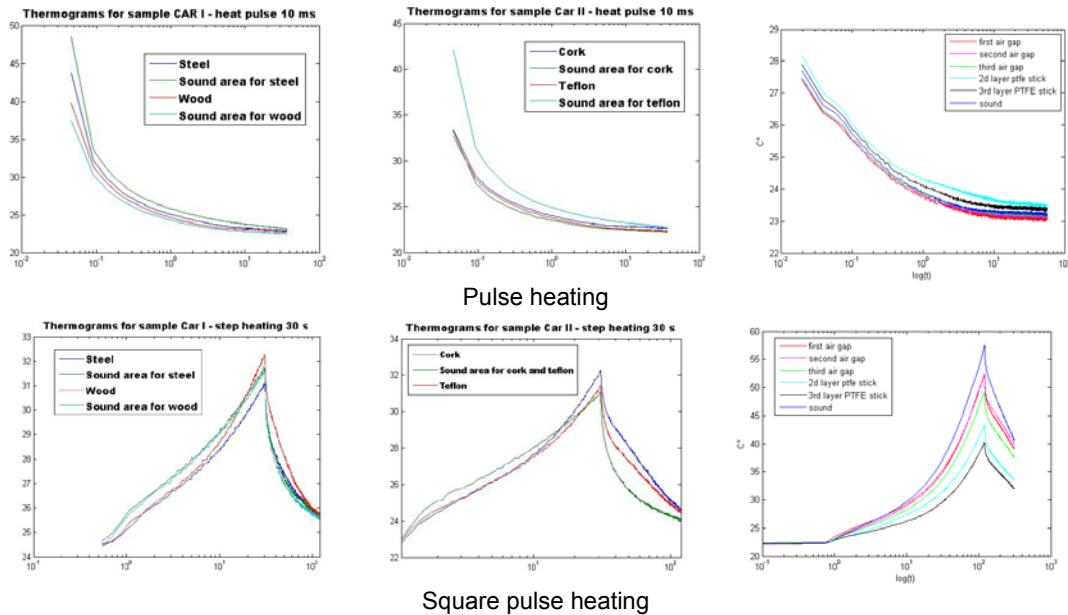


Fig. 6. Pulse (top) and square pulse heating (bottom) thermograms extracted from experimental thermal image sequences

In the case of pulsed heating excitation on CAR samples (Figure 6, top), the thermal profiles for all types of defects qualitatively follow the same behaviour predicted by the simulation (Fig. 5 left), i.e. the less effusive materials (cork and wood, see Table 2) produce a positive contrast and the more effusive (steel and Teflon®, see Table 2) a negative contrast with respect to the sound areas (individually selected next to the defective areas to minimize non-uniformities). In the case of square heating however, the situation is different for the case of more effusive materials. For instance, the thermal profile for steel (Figure 6, bottom-left) follows the behaviour predicted by simulation during heating but this trend is inverted during the cooling stage. This is probably due to the presence of a thermal resistance (probably

air) in the interface between the steel and the epoxy. Furthermore, the actual size of this defect is less than the one considered for numerical simulations. In addition, the epoxy layer is probably more than 1 mm thickness due to fabrication conditions in laboratory (i.e. skilled personnel generally succeed in having a finished thickness between 0.5 to 1 mm).

For the Teflon® defect, a similar behaviour can be noticed, although in this case, the trend is inverted before the heating stage has finished and continues during the cooling stage. For such defect in Teflon® it is expected to have a positive contrast versus sound area when only its thermal resistance is considered and presence of lateral epoxy resin is neglected, in particular if it has a negligible volume, hypothesis commonly adopted for 1D geometries for flaw in composites. Nevertheless, in this 3D approach, defect is inserted in an epoxy layer of a non-negligible thickness, so thermal effusivity of epoxy resin and CFRP versus Teflon needs to be considered. Table 2 reports the main thermal characteristics of the studied material (thermal resistances and effusivities).

Table 2. Thermal resistance and effusivity for the materials.

Material	Thermal resitivity (see table 1 for depth) in [W.°C <sup>-1</sup> ]	Thermal effusivity in [W.s <sup>1/2</sup> .m <sup>-2</sup> .K <sup>-1</sup> ]	Effusivity ratio: CFRP/Material type	Effusivity Ratio: Epoxy resin/Material type
CFRP	0.0017	948.5	1.00	0.57
Epoxy	0.0050	542.5	1.75	1.00
Air	0.0413	5.5	173.65	99.31
Water	0.0017	1582.6	0.60	0.34
Wood	0.0067	413.5	2.29	1.31
Teflon	0.0043	736.8	1.29	0.74
Cork	0.0256	91.8	10.33	5.91
Steel	6.62E-05	7640.9	0.12	0.07

From Table 2 it is noticed that Teflon is the only material considered herein for which the effusivity ratio with respect to CFRP is higher than 1 ( $e_{cfRP/Teflon}=1.3$ ) and the effusivity ratio with respect to epoxy resin is lower than 1 ( $e_{epoxy/Teflon}=0.7$ ). This could explain the differences between 3D simulated analysis and the experimental results

These experimental and simulated thermal profiles are next used to test the inverse approach used.

For wood\_car, we address defects like Teflon stick, that can be considered in that case as pure thermal resistance but also air gaps in the support layer (wood plank) with non-negligible thermal inertia.

### 3.2. Defects detection and mapping

Singular value decomposition (SVD) employed in a previous study [5] was used for defect detection and localization on infrared image sequence.

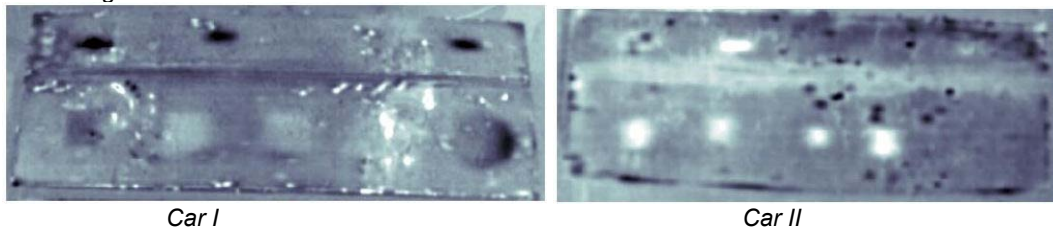
Singular value decomposition (SVD) is an interesting tool for the extraction of the spatial and temporal information from a thermal image sequence in a compact or simplified manner. The SVD of an  $M \times N$  matrix  $\mathbf{A}$  ( $M > N$ ) can be calculated as follows [6-7]:

$$\mathbf{A} = \mathbf{U}\mathbf{R}\mathbf{V}^T \quad (1)$$

where  $\mathbf{U}$  is an  $M \times N$  orthogonal matrix,  $\mathbf{R}$  being a diagonal  $N \times N$  matrix (with the singular values of  $\mathbf{A}$  in the diagonal) and  $\mathbf{V}^T$  is the transpose of an  $N \times N$  orthogonal matrix (characteristic time).

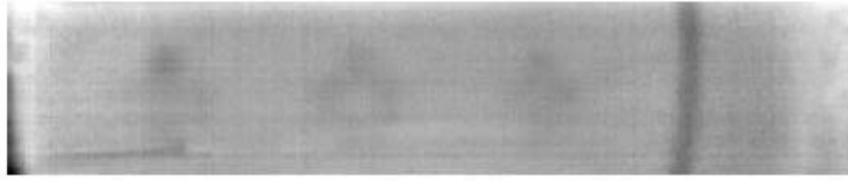
After rearranging the thermal image for every time as columns in  $\mathbf{A}$  and applying the SVD, the columns of  $\mathbf{U}$  represent a set of orthogonal statistical modes known as empirical orthogonal functions (EOF) that describes spatial variations of data. On the other hand, the principal components (PCs), which represent time variations, are arranged row-wise in matrix  $\mathbf{V}^T$ . The first EOF will represent the most characteristic variability of the data; the second EOF will contain the second most important variability, and so on. Usually, original data can be adequately represented with only a few EOFs [7-8]. SVD computations were performed on experimental thermal images sequences for pulse and square heating acquired at different frequencies. It has to be noticed that for pulse heating only the thermal relaxation is recorded and for the square heating thermal image sequence starts at the beginning of the sample heating.

Fig. 7 shows defect localization obtained on laboratory samples CAR I, CAR II and Wood\_Car with optical thermal pulse excitation of 10 ms on the raw surface without cleaning in the case of CAR samples (see Fig. 1). Even in this non favourable configuration defects can be detected.



Car I

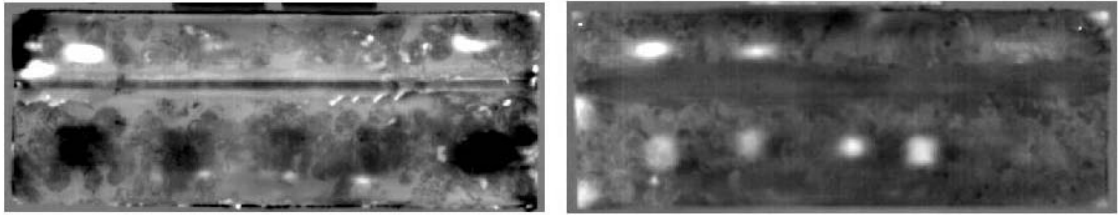
Car II



Wood\_car

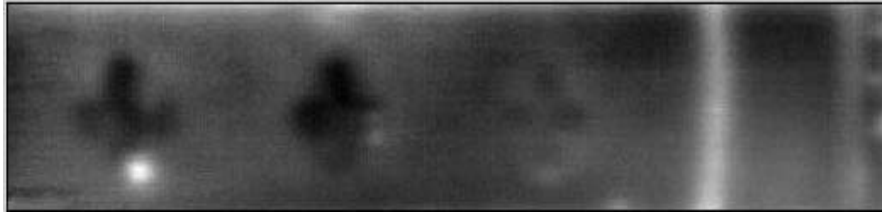
**Fig. 7.** Results with principal component analysis on pulsed thermography data obtained from laboratory experiments using the photographic flashes on specimens CAR I (left) and CAR II (right).

Fig. 8 shows defect localization obtained on laboratory samples CAR I, CAR II and wood\_car with optical square heating excitation of 30 s and 120s on the raw surface.



Car I

Car II



Wood\_car

**Fig. 8.** Results with principal component analysis on square heating thermography data obtained from laboratory experiments using the photographic flashes on specimens CAR I (left) and CAR II (right).

In the following paragraph, faulty and sound areas localised by using these EOF maps were used for computation.

#### 4. Defects characterization using an inverse method

##### 4.1. Thermal Model

The thermal model approach is based on a multilayer 1D thermal quadrupole model [8] (Eq. 2). It is studied for defect detection and characterization by computing thermal properties identification and glue layer thickness estimation procedure:

$$\begin{bmatrix} \theta_{in} \\ \varphi_{in} \end{bmatrix} = \prod_i^{N\_Layers} M_i \begin{bmatrix} \theta_{out} \\ \varphi_{out} \end{bmatrix} \text{ With: } q_i = \sqrt{\frac{p}{\alpha_i}} \text{ and } M_i = \begin{pmatrix} \cosh(q_i e_i) & \frac{\sinh(q_i e_i)}{k_i q_i} \\ k_i q_i \sinh(q_i e_i) & \cosh(q_i e_i) \end{pmatrix} \quad (2)$$

Eq 2 is expressed in the Laplace domain and parameter's estimations are carried out in time domain by using the Stehfest algorithm [11]. The inverse problem is expressed in the least-squares sense (Eq. 3) and consists in finding the optimal solution that minimizes the expression:

$$S = \sum_{i=1}^M [T_{meas,i} - T_{estim,i}]^2 \quad (3)$$

where  $T_{meas}$  is the measured temperature, and  $T_{estim}$  is the estimated temperature, both parameters are computed at each time sampling thanks to the heat transfer modeling presented in Eq. 2.

## 4.2. Sensitivity study

In order to carry out a reliable estimation of the defective and sound area thermal properties but also of layer thickness, the model variability to each parameter of interest was studied. Reduced sensitivity functions are defined as the first derivative of the temperature with respect to the parameters (see Eq. 4).

$$S(P_i) = P_i \frac{\partial T}{\partial P_i} \quad (4)$$

Where, parameter vector  $P = [e_2, a_2, k_2, \rho C_2, \varphi_0, h_1, Te_1]$  contain parameters of interest. The following results focus on the characterization model sensitivity at second layer thermal parameters and thickness.

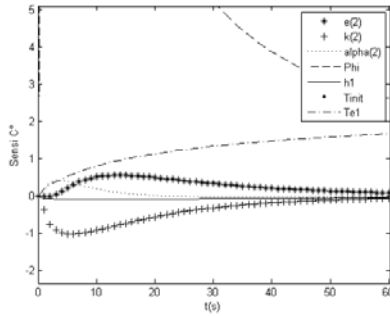


Fig. 9. Reduced sensitivity functions for a pulse heating

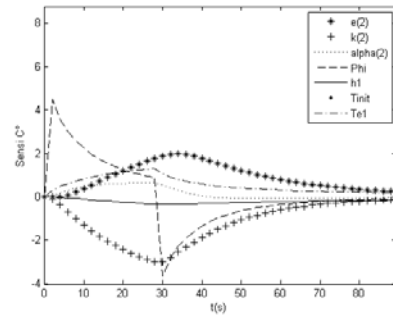


Fig. 10. Reduced sensitivity functions for a square pulse heating

Figure 9 show the reduced sensitivity functions for pulse heating. As detailed in [9], a parameter can be estimated if its sensitivity function represents at least 1% of the total response. It can be shown that for this kind of excitation the heat flux have to be powerful enough to maximize the sensitivity function; in the present case the model is sensible to each parameter during a limited time period.

Figure 10 show the reduced sensitivity functions for a 30s square pulse heating. It can be deduced that if the step section of figure 10 is long enough, the heat flux importance decrease while the sensitivity to other parameters increase. It is of particular interest when one want to reduce the weight of heat flux determination for parameter estimation. If the heat flux is known, the release part is the part where the useful parameters can be estimated. For a correct estimation [9], parameters have to be uncorrelated in time. For this, the sensitivity matrix have to be construct Eq. 5.

$$J(P) = \begin{bmatrix} \frac{\partial}{\partial P_1} \\ \frac{\partial}{\partial P_2} \\ \dots \\ \frac{\partial}{\partial P_n} \end{bmatrix} [T_1 \quad T_2 \quad \dots \quad T_i] = \left[ \frac{\partial T^T(P)}{\partial P} \right]^T \quad (5)$$

The identifiable condition is defined [10] as Eq. 6.

$$\left| J^T J \right| \neq 0 \quad (6)$$

Where  $\left| \cdot \right|$  is the determinant, if Eq. 5. is near zero the problem is denoted *ill-conditioned* and the Gauss-Newton iterative technique for identification can't be used [10], in this case Levenberg-Marquard Method is used.

From Eq.5 and [10], it can be observed that, in order to have an accurate identification method, it is necessary to find a time gap, with a constant number of steps that maximizes Eq. 5. For instance, for a time measurement of 90 s sampled at 10 Hz and the parameters vectors  $P = [\alpha_2, k_2]$  (other parameters are assumed to be known), the identifiable condition is studied for a time-window of 5 s (50 steps), values of identifiable condition are collected by

moving this time window .Figure 11 and 12 show the identifiable condition values versus the last frame of the time-window.

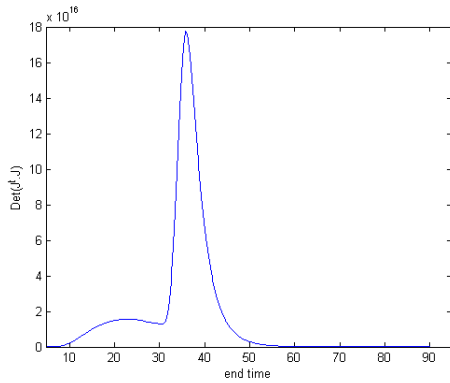


Fig. 11. identifiable condition versus the time-window end for a 30 s square pulse heating

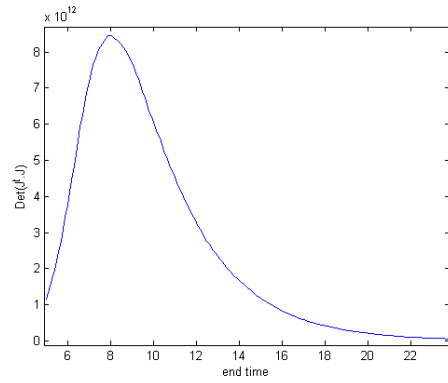


Fig. 12. identifiable condition versus the time-window end for a pulse heating

The function decreases when the parameters sensitivity function approximate zero or when it stagnates. The pulse heating excitation allows parameters estimation during a reduced time and for a sampling frequency high enough. Square pulse heating excitation have the same shape as the step function during the first 30 s, but have higher sensitivity level when the thermal relaxation part is studied.

### 4.3. Application to simulated and experimental data: Results analysis

#### 4.3.1. Simulated Data

A first estimation procedure, using our thermal model and considering sensitivity analysis results have been carried out with simulated data. Relative errors were calculated thanks to standard thermal properties values shown in Table 1 and used for numerical simulations. The inverse problem Eq.(3) is solved using a Levenberg-Marquart algorithm [12].

Table 3 show the estimated data and the relative error for each materials and excitation

**Table 3 Result of estimation procedure**

Pulse heating		
Second layer	Estimated conductivity	Relative error
Sound	0.21	6.76%
steel	2.11	86%
teflon	0.27	18.7%
Crock	0.046	19.5%
wood	0.169	12.8%
air	0.0243	0.5%
water	0.56	5.45%
Square pulse heating		
Second layer	Estimated conductivity	Relative error
Sound	0.18	8%
steel	4.01	73%
teflon	0.21	5.4%
Crock	0.045	16.15%
wood	0.149	0.5%
air	0.032	35.5%
water	0.45	23.54%

These data show that estimated thermal conductivity values can be obtained with a relative error between 5 and 20%, except for the steel, that has the lowest thermal effusivity ratio versus glue. When thickness is added to parameters vector (to be identified), relative error for conductivity estimation increase by more than 50%. In the present results, thickness is known so it induces better estimation procedure.

Nevertheless, to complete the study of this estimation procedure the variability of the method versus temperature measurement noise was studied. Figure 13 and 14 show estimation relative errors induced by a white noise.

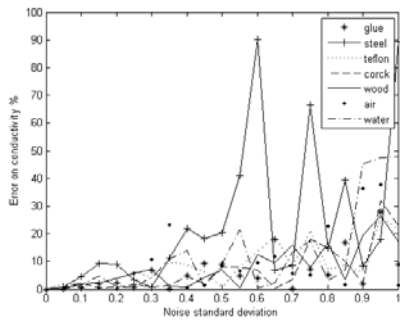


**Fig.13** Relative error versus noise measurement for a pulse heating

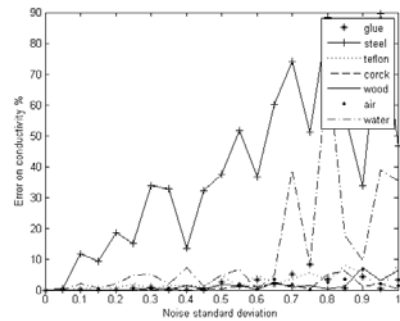


**Fig.14** Relative error versus noise measurement for a square pulse heating

Except for steel materials, the square pulse heating is less influenced by the noise level than pulse heating approach.

#### 4.3.2. Experimental Data

To test the model, an estimation campaign was carried out with experimental data presented in paragraph 3.1. It has to be noticed that in that experimental configuration glue layer thickness over flaws and in sound areas was not known. Hence, according to the model performances presented in previous paragraphs, we are in such test case with deteriorated domain for parameters identification.

#### 4.3.3. Thermal excitation by square pulse

Table 4 shows results obtained for a square pulse heating thermal excitation on samples.

**Table 4** Estimation results for square pulse heating

Wood Carb sample		
Flaw	Estimated conductivity	Thickness in mm
Sound (glue)	1.66	1.5
First PTFE stick	1.8	0.9
Carb I sample		
Flaw	Estimated conductivity	Thickness in mm
steel	1.8	0.9
wood	5	0.9
Sound (glue)	1.8	0.9
Carb II sample		
Flaw	Estimated conductivity	Thickness in mm
Cork	1.8	5.2
Teflon	1.9	4.2
Sound (glue)	1.6	2.7

Except for Carb II sample, identified thickness is in an interval of values in agreement with what can be observed making direct measurement on sides of samples. Identified thermal conductivities are more closed to equivalent values due to estimated thickness values, more closed to a one layer equivalent to two layers made of different materials : defect + glue. For Carb II, results are also more affected by measurement noise.

#### 4.3.4. Thermal excitation by Pulse heating

Table 5 shows results obtained for a pulse heating thermal excitation on samples.

**Table 5 Estimation results for a pulse heating**

<b>Wood Carb sample</b>		
Flaw	Estimated conductivity	Thickness in mm
Sound	4.39	4.6
First PTFE stick	5	0.9
<b>Carb I sample</b>		
Flaw	Estimated conductivity	Thickness in mm
steel	1.9	1.4
wood	1.6	8.4
Sound	1.9	4.1
<b>Carb II sample</b>		
Flaw	Estimated conductivity	Thickness in mm
Cork	5	1.5
Teflon	3.4	6.4
Sound	3.01	6.4

As noticed and predicted during the model presentation and its parameter sensitivity study, results obtained with such type of thermal excitation are more affected by measurement noise. Results obtained with Carb II sample are again the more affected by measurement noise.

## 5. Conclusion and perspectives

Two types of thermal excitation have been studied. Defect location is rapidly performed thanks to SVD. A 1D multi-layer thermal quadrupole model coupled with an estimation procedure was studied and used to characterize the defects and the glue layer thickness variability. As regard to the sensitivity study, the model is quite reliable when thickness is known and practically insensitive to noise measurement up to a standard deviation of 0.5, with the exception of steel. Secondly, it was shown that square pulse is the most relevant kind of excitation to characterize the glue layer (no more than 35% of relative error level and a low dependence at noise measurement observed on numerical simulation data). Nevertheless, experimental results diverge from estimations, poor performances were observed compared to numerical simulation data. Complementary investigations are required, in particular on glue and defect independent thermal characterization. As perspectives and after model enhancement (for instance by adding thermal resistances), parallel computing will be studied to enhance the processing time as well as data fusion, thanks to image processing in order to allow the use of simplified models when no defect are detected. As improvement of the quadrupole model, a view form can be added to take in account the 3D diffusion effect in the proposed model. For materials with low effusivity ratio versus glue layer 2D model will be investigated. Another prospect is to compare the model to thermal contrast and pulse phase approaches and combine them to improve the estimation procedure.

## REFERENCES

- [1] ACI Committee 440.2R02-08. "Guide for the Design and Construction of Externally Bonded Systems for Strengthening Concrete Structures", American Concrete Institute, Michigan, U.S.A., 2008.
- [2] AFGC. (2007). "Réparation et renforcement des structures en béton au moyen des matériaux composites – Recommandations provisoires", Bulletin scientifique et technique de l'AFGC. (in French).
- [3] Fib Task Group 9.3. (2001) Externally bonded FRP reinforcement for RC structures, fib bulletin 14, Lausanne, Switzerland.
- [4] J. Dumoulin, F. Taillade, Ch. Aubagnac, K. Benzarti, M. Quiertant, « Infrared Thermography for the Nondestructive Inspection of CFRP Strenghtening », Concrete International, volume 33, issue 4, pp. 54-58, April 2011.
- [5] Dumoulin J., Ibarra-Castanedo C., Quiertant M., Taillade F., Bendada A. and Maldague X., « Evaluation of FRP gluing on concrete structures by active infrared thermography », QIRT2010 (Quantitative Infrared Thermography Conference), Québec City, Canada, 26-30 July 2010.
- [6] Rajic N., "Principal component thermography for flaw contrast enhancement and flaw depth characterization in composite structures", Composite Structures, vol 58, pp 521–528, 2002.
- [7] Marinetti S., Grinzato E., Bison P. G., Bozzi E., Chimenti M., Pieri G. And Salvetti O. "Statistical analysis of IR thermographic sequences by PCA," Infrared Physics & Technology vol 46 pp 85–91, 2004.
- [8] Maillet D., André S., Batsale J. C., Degiovanni A. and Moyne C., "Thermal Quadrupoles", Wiley, Chichester, 2000.
- [9] FAUGEROUX.O et al, "Caracterisation thermophysique de revetements par methode photothermique impulsionnel le en face avant", International Journal of Thermal Sciences, volume 43, pp 383–401, 2004.
- [10] OZISIK.M.N, "Inverse heat transfer", Taylor & Francis, 2000.
- [11] STEHFEST.H, "Algorithm 368 : Numerical inversion of laplace transform", Communication of the ACM 13 pp 47–49, 1970.
- [12] LEVENBERG.K, "A method for the solution of certain non-linear problems in least-squares" Appl. Math, volume 2, pp 164–168, 1944.